AIAA JOURNAL
Vol. 42, No. 11, November 2004

Numerical Studies of Laser-Induced Energy Deposition for Supersonic Flow Control

Ramnath Kandala* and Graham V. Candler†
University of Minnesota, Minneapolis, Minnesota 55455

This work deals with the computational study of localized laser energy deposition in supersonic flows. A model for Nd:YAG laser energy deposition in air has been developed for this purpose. It is designed to predict the fluid dynamic effects of the energy deposition process in supersonic flows. The key physical processes are captured, including inverse bremsstrahlung absorption, evolution of the plasma shape and structure, air breakdown chemistry, and the subsequent fluid dynamics. The model is validated using measurements of experiments done in quiescent air. The effects of energy deposition in three-dimensional supersonic flow past sphere and a flow with Edney type IV shock-shock interaction were studied. The energy deposition was found to be effective in reducing the peak surface pressure, but not as effective in lowering the surface heat-transfer rate. In the case of flow with Edney type IV shock-shock interaction, a study was performed to find the optimal location for the energy deposition, for which there is maximum decrease in the surface pressure.

Nomenclature

A, B	=	constants of reflectivity
$\boldsymbol{C}$	=	Jacobian matrix
c	=	speed of light in vacuum, m s^{-1}
E	=	energy, J m^{-3}
e	=	specific energy, J kg^{-1}
e^-	=	electron
$\boldsymbol{F}$	=	flux in axial direction
$\boldsymbol{G}$	=	flux in radial direction
g_e	=	electron thermal speed, m s^{-1}
h	=	Planck constant, J s
h_s	=	specific enthalpy, J kg^{-1}
I	=	intensity, W m^{-2}
k	=	Boltzmann constant, J K^{-1}
k_e	=	electron thermal conductivity, J m^{-1} s^{-1} K^{-1}
L_p	=	axial length of plasma region, m
M	=	heavy particle
m	=	mass, kg
n_e	=	electron number density, m^{-3}
p	=	pressure, Pa
Q	=	cross section of absorption, m^2
Q_{en}	=	average collision cross section, m^2
Q_{h-e}	=	heavy particle-electron energy exchange, J m^{-3} s^{-1}
Q_r	=	radiative energy source, J m^{-3} s^{-1}
Q_{T-v}	=	translation-vibration energy exchange, J m^{-3} s^{-1}
Q_{v-e}	=	vibration-electron energy exchange, J m^{-3} s^{-1}
q	=	heat flux, J m^{-2} s^{-1}
q_{abs}	=	average absorption rate, J m^{-3} s^{-1}
r	=	radial direction, m
T	=	temperature, K
t	=	time, s
$\boldsymbol{U}$	=	vector of conserved variables
$\boldsymbol{u}$	=	velocity, m s^{-1}
$\boldsymbol{v}$	=	diffusion velocity, m s^{-1}
$\boldsymbol{W}$	=	source vector
w	=	generation rate, kg m^{-3} s^{-1}
x	=	axial direction, m
Z	=	fraction of ionization
α	=	fraction of reflected energy incident on adjacent cell
β	=	arc angle about leading edge of sphere
δ_{eh}	=	inelastic loss factor
ϵ_I	=	ionization potential, eV
κ_a	=	absorptivity coefficient, m^{-1}
κ_r	=	reflectivity coefficient
λ	=	wavelength, m
ν	=	frequency, s^{-1}
ν_{eh}	=	electron-heavy particle collision frequency, s^{-1}
ρ	=	density, kg m^{-3}
$\tilde{\tau}$	=	shear-stress tensor, N m^{-2}

Subscripts

e	=	electron
h	=	heavy particle
i, j	=	cell (i, j)
s	=	specie s
v	=	vibration

Superscript

n	=	time step

Presented as Paper 2003-1052 at the 41st Aerospace Sciences Meeting, Reno, NV, 6–9 January 2003; received 2 December 2003; revision received 10 June 2004; accepted for publication 14 June 2004.

*Research Assistant, Aerospace Engineering and Mechanics; ramnath@aem.umn.edu. Student Member AIAA.

†Professor, Aerospace Engineering and Mechanics. Associate Fellow AIAA.

Introduction

WHEN a powerful laser is focused into air or onto a target, an intense spark or plasma is formed. This plasma can be used for a variety of aerospace applications including flow control,[1,2] ignition of combustion gases,[3] laser thrusters,[4] and propulsion systems.[5] In the present case, we are interested in laser energy deposition as a means of localized flow control. Energy deposition increases the gas temperature in the plasma region and produces a pressure wave, which can be used to modify the local flow to achieve the desired effect. For example, experiments[1] have shown that the detrimental effects of a shock-shock interaction (which can occur on an air vehicle during maneuver) can be mitigated using localized energy deposition.

In this work, we use numerical simulations to study the effects of Nd:YAG laser energy deposition in supersonic flows past blunt bodies, using computational simulations. The simulation of the energy deposition process was performed using a numerical model

that we have developed. This model captures the essential features of the energy deposition process, namely, absorption of laser radiation, the subsequent plasma formation, and the fluid dynamics that result from it. The flowfield is described by the Navier–Stokes equations, with extensions to include the effects of nonequilibrium thermochemistry and the energy source terms. An 11-species air chemistry model with finite-rate chemical kinetics is used to simulate the plasma. We use this model to study energy deposition in quiescent air, supersonic flow past a sphere, and flows with Edney type IV shock–shock interaction. We compare our calculations with the results of experiments conducted at Rutgers University.[1]

Laser Spark and Detonation Physics

Laser energy deposition into a gas is achieved by focusing a pulsed laser beam onto a small focal volume. The resulting process can be described by the following progressive steps (Fig. 1): initial release of electrons by multiphoton ionization, ionization of the gas in the focal region by the cascade release of electrons, absorption of laser energy by the gaseous plasma, rapid expansion of the plasma and detonation wave formation, and the propagation of the pressure wave into the surrounding gas.

There are two mechanisms for electron generation and growth.[6] The first mechanism, called multiphoton ionization (MPI), involves the simultaneous absorption by an atom or molecule of a sufficient number of photons to cause its ionization. MPI is described by the reaction:

$$M + mh\nu \rightarrow M^+ + e^-$$

where $mh\nu$ represents the energy absorbed from m photons of energy $h\nu$. If ϵ_I is the ionization potential, the number of photons absorbed must exceed $\epsilon_I / h\nu$. In this process, the electron number density increases linearly with time. The ionization potential of most gases is greater than 10 eV. Hence multiple photon collisions on an atom or molecule in the gas medium are needed because the energy required to release an electron is greater than the energy absorbed by a collision with a single photon ($\simeq$1 eV).

The second mechanism involves absorption of laser radiation by electrons as a result of electron-neutral inverse bremsstrahlung collisions. This is the reverse of the bremsstrahlung process in which high-energy electrons, upon traversing a gas or solid, emit radiation as they slow down. If the electrons gain energy greater than the ionization energy of the gas, they can impact ionize the gas or solid through the reaction

$$M + e^- \rightarrow M^+ + 2e^-$$

This reaction will lead to cascade ionization, that is, the electron concentration will increase exponentially with time.

Once the cascade ionization is underway, the resultant plasma absorbs the laser energy to a considerable degree. Raizer[7] gives a detailed description of this absorption mechanism. The primary cascade ionization occurs in the narrowest region of the converging light, owing to the high intensity (Fig. 1b). But the absorption is not confined to a single volume (characterized by the beam radius at the focal point) in which the primary cascade ionization has occurred. Instead, once the degree of ionization reaches a high value, cascade ionization occurs in the adjacent region where the light intensity is lower. As this new region is ionized, it becomes opaque to the laser light and absorbs the energy. In this fashion, the absorption region is continuously displaced towards the lens, producing a wave of light absorption and gas heating. Raizer[7] suggests that the thermal radiation from the strongly heated region is absorbed by the cooler gas, which in turn acquires the ability to absorb light. This process is termed the radiative mechanism. The outcome of this effect is the distribution of the laser energy over a larger volume, which reduces the peak temperature.

In the final step of energy deposition, the laser pulse ends, and the plasma recombines. The focal region of the laser light has been substantially heated leaving behind a region with higher specific internal energy as compared to before the pulse. The pressure has correspondingly increased, and conversely the density has decreased as a result of the expansion and rarefaction process. This increase in pressure and temperature is the fluid dynamic effect of the energy deposition process.

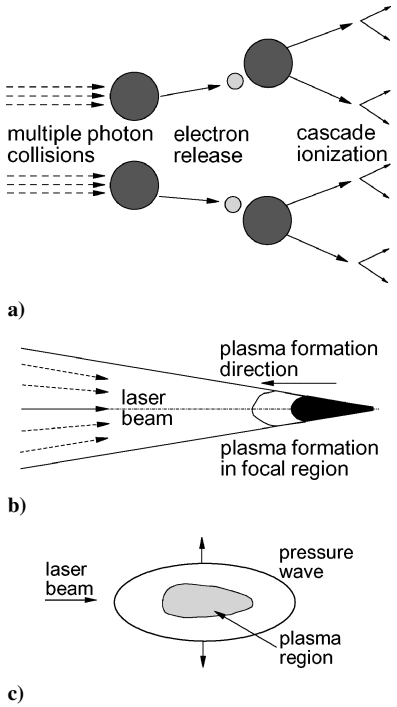

Fig. 1 Schematic showing the sequence of steps leading to laser energy deposition in air.

Mathematical Formulation

The numerical model has to capture the features of the plasma region (the chemical composition and the state of the gas) that affect the fluid dynamics. At the same time, it is not required to simulate the interaction between laser radiation and gas particles in excessive detail. Therefore, the model was designed such that it captures the key features required for flow control studies, while not being overly complicated.

Plasma Formation Model

The plasma formation involves multiphoton ionization, inverse bremsstrahlung absorption and the displacement of the absorption region. It has been shown through analytical[7] and experimental[8] means that, for gases at atmospheric and higher pressures, cascade ionization dominates. Hence we neglect multiphoton ionization in our modeling. Instead, a small number of seed electrons are used to initiate the electron cascade by absorbing the laser light at the beginning of the simulation. The inverse bremsstrahlung absorption is modeled using the absorptivity coefficient κ_a. The displacement of the absorption region is accounted for by introducing the concept of reflectivity, characterized by coefficient κ_r. As the plasma density increases, the laser light is scattered as a result of reflection. Some of this light is reabsorbed by the adjacent cooler gas to trigger cascade ionization in those regions. Therefore reflectivity is an empirical formulation that limits the degree of ionization of any region, enables the displacement of the absorption region towards the lens, and accounts for the loss of energy caused by radiation.

The laser beam is focused using a converging lens as shown in Fig. 2. We divide the focal volume into discrete cells. Each cell receives energy from two sources: the laser beam, and a fraction of the light reflected by the adjacent cells with higher plasma density. This energy is in turn absorbed, reflected, or transmitted by the cell as illustrated in Fig. 2. Although absorption of transmitted light dominates the early part of plasma formation, reflection becomes important as the plasma density increases.

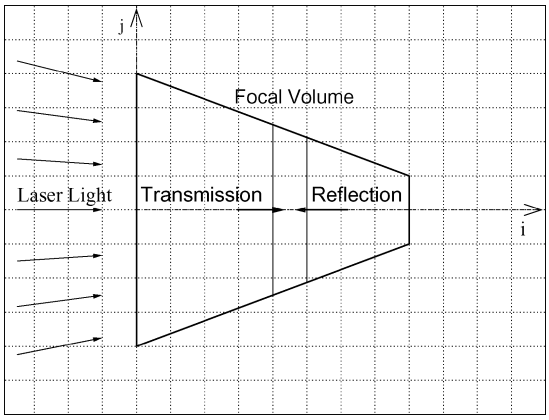

Fig. 2 Schematic of the model used for energy addition in the focal region.

Because of laser absorption, the intensity of the laser beam I varies in the direction of laser propagation x (Ref. 4):

$$\frac{\mathrm{d}I}{\mathrm{d}x} = -\kappa_a I$$

By integrating the preceding equation and assuming a constant $\kappa_{a_{i,j}}$ over a grid cell $q_{\mathrm{abs}_{i,j}}$ the average absorption rate inside a cell of width $\Delta x_{i,j}$, along the direction of light propagation (i direction), as a function of the intensity is

$$q_{\mathrm{abs}_{i,j}} = I_{i,j}\frac{1-\exp\left(-\kappa_{a_{i,j}}\Delta x_{i,j}\right)}{\Delta x_{i,j}}$$

where

$$I_{i,j} = \left(1-\kappa_{r_{i,j}}\right)I_{s_{i,j}} + \alpha_{i,j}\kappa_{r_{i+1,j}}I_{s_{i+1,j}}$$

$I_{s_{i,j}}$ is the intensity of the incident light for the cell (i, j) and $\alpha_{i,j}$ is the fraction of the energy from the cell $(i+1, j)$ that reaches the cell (i, j). The parameter α ensures that only a part of the reflected laser light is self-absorbed, whereas the rest is assumed to be lost as a result of emission. Assuming that the laser light is scattered uniformly in all directions, α is taken to be the ratio of the surface area of the face common to the cells (i, j) and $(i+1, j)$ to the total surface area of the cell $(i+1, j)$. κ_a depends on electron density, electron temperature, and ion/neutral densities. For a weakly ionized gas, we can neglect inverse bremsstrahlung absorption caused by electron-ion collisions and assume a constant density for neutral particles. Thus, we simplify the expression for electron-neutral absorption coefficient given in Ref. 6:

$$\kappa_a = Qn_e[1-\exp(-hc/\lambda kT_e)]$$

The plasma is transparent to the laser light in the initial stages, but it becomes opaque gradually. Thus, the reflectivity coefficient κ_r depends on the fraction of ionization Z and varies between 0 and 1. Because Z varies exponentially with time, we use a logarithmic function to relate it to κ_r:

$$\kappa_r = A[\log(Z) + B]$$

The unknowns in the preceding analysis are Q, the characteristic area of cross section, and A and B, the constants for the reflectivity coefficient. Their values determine the energy absorbed and the shape and the structure of the plasma region. Indirectly, these parameters also determine the fraction of the incident laser energy, which is transmitted past the focal region without being absorbed. There are no direct measurements of Q, A, and B for Nd:YAG laser absorption in air. Therefore, we determine their values by matching the flow properties of the resulting pressure wave to experiments.

Chemical Kinetics

In this flow we assume that 11 species might be present in appreciable quantities: N_2, O_2, NO, N, O, N_2^+, O_2^+, NO^+, N^+, O^+, and electrons. After the laser energy is deposited, the electron temperature rises sharply, leading to many thermochemical processes. A chemical kinetics model for two-temperature air (translational-rotational and electron temperatures) was developed at Stanford University[9] and has been used to successfully analyze dc and pulsed discharge experiments.[10] This model is ideally suited for this problem and is used in the present work.

Conservation Equations

In this section we briefly describe the governing equations. These equations are described in a greater detail in Ref. 11. We solve mass conservation equations for each of the 11 species and momentum conservation equations for the axial and radial momenta and energy conservation equations for total, vibrational, and electron energies. The mass conservation equation for chemical species s is given by

$$\frac{\partial \rho_s}{\partial t} + \nabla\cdot(\rho_s \boldsymbol{u}) = -\nabla\cdot(\rho_s \boldsymbol{v}_s) + w_s$$

The mass-averaged momentum conservation equation is written as

$$\frac{\partial}{\partial t}(\rho \boldsymbol{u}) + \nabla\cdot(\rho \boldsymbol{u}\otimes\boldsymbol{u}) = -\nabla p - \nabla\cdot\tilde{\tau}$$

The conservation equations of the total energy, vibrational energy, and the electron energy are given by

$$\frac{\partial E}{\partial t} + \nabla\cdot[(E+p)\boldsymbol{u})] = -\nabla\cdot(\boldsymbol{q}+\boldsymbol{q}_v+\boldsymbol{q}_e) - \nabla\cdot(\boldsymbol{u}\cdot\tilde{\tau}) - \nabla\cdot\sum_{s=1}^{n}(\boldsymbol{v}_s\rho_s h_s) + Q_r$$

$$\frac{\partial E_v}{\partial t} + \nabla\cdot(E_v\boldsymbol{u}) = -\nabla\cdot\boldsymbol{q}_v - \nabla\cdot\sum_{s=1}^{n}\boldsymbol{v}_s E_{v,s} + Q_{T-v} + Q_{e-v} + \sum_{s=1}^{n} w_s e_{v,s}$$

$$\frac{\partial E_e}{\partial t} + \nabla\cdot[(E_e+p_e)(\boldsymbol{u}+\boldsymbol{v}_e)] = -\nabla\cdot\boldsymbol{q}_e - Q_{h-e} - Q_{v-e} + Q_r + w_e e_e$$

The variation of electron temperature is the most important feature in these flows. Hence, the breakdown of the terms in the electron energy conservation equation are discussed here. The radiative energy addition and loss are represented in the electron energy conservation equation by Q_r. In the present case Q_r is equal to q_{abs}. The conductive flux of electron energy is $\boldsymbol{q}_e = -k_e\nabla\cdot T_e$. The thermal conductivity of electrons k_e is taken from Mitchner and Kruger.[12] The heavy particle-electron energy transfer Q_{h-e} is

$$Q_{h-e} = n_e\sum_h 3k(T_e - T)\left(\frac{m_e}{m_h}\right)\delta_{\mathrm{eh}}\nu_{\mathrm{eh}}$$

where T is the total temperature and m_e and m_h represent the mass of electrons and heavy particles respectively. The expressions for δ_{eh} and ν_{eh} are taken from Ref. 9. The collision frequency is approximated by the electron-neutral collision frequency:

$$\nu_{\mathrm{eh}} = (p/kT)g_e Q_{\mathrm{en}}$$

where $g_e = \sqrt{(8kT_e/\pi m_e)}$ is the electron thermal speed and Q_{en} is the average cross-section taken to be 10^{-15} cm^2 as per Ref. 10. The vibrational-electron energy transfer rate Q_{v-e} is taken from Ref. 13.

Numerical Aspects

The initiation of electron cascade is characterized by timescales of 1 ns or less because the electron-impact ionization process is extremely fast at high electron temperatures. On the other hand, the pressure wave expansion around the plasma region occurs at a timescale of about 10 μs. Thus, the range of timescales is over four orders of magnitude. To handle this large disparity in characteristic timescales, we would usually use an implicit time-integration method. However, for this problem a complete linearization would be very expensive. (We solve 16 conservation equations, and the cost of evaluating the Jacobians and inverting the system scales with the square of the number of equations.) Therefore, for our simulations we linearize only those terms that are relatively fast, which results in a simple and inexpensive semi-implicit method that substantially reduces the cost of the calculations.

The relatively fast terms include some species production terms, the internal energy relaxation, and the electron heating source terms. Therefore, we split the source vector $\boldsymbol{W}$ into these terms W_{fast} and all of the other terms W_{slow}. The conservation equations are then written in axisymmetric coordinates as

$$\frac{\partial U}{\partial t}+\frac{\partial F}{\partial x}+\frac{1}{r}\frac{\partial rG}{\partial r}=W_{\text{fast}}+W_{\text{slow}}$$

We linearize W_{fast} in time:

$$W_{\text{fast}}^{n+1}=W_{\text{fast}}^{n}+C_{\text{fast}}^{n}\delta U^{n}+\mathcal{O}(\Delta t^{2})$$

where C_{fast} is the Jacobian of W_{fast} with respect to U, and $\delta U^{n}=U^{n+1}-U^{n}$. C_{fast} is a simple matrix that can be inverted analytically. Then, the solution is integrated in time using

$$\delta U^{n+1}=\left(I-\Delta t C_{\text{fast}}^{n}\right)^{-1}\Delta t\left[\left(W_{\text{fast}}^{n}+W_{\text{slow}}^{n}\right)-\left(\frac{\partial F^{n}}{\partial x}+\frac{1}{r}\frac{\partial rG^{n}}{\partial r}\right)\right]$$

This approach increases the stable time step by up to a factor of 50 compared to an explicit Euler method, at essentially no additional cost.

Model Validation

To validate the model, we have simulated the plasma generated by a single laser pulse in quiescent air and compared these simulations with the results from the experiments.[1] An Nd:YAG laser with 532-nm wavelength, 108-mJ pulse energy, and a pulse width of 20 ns was used as input in the computations. The laser beam radius was 10 mm, and the focal length of the converging lens was 100 mm. The laser beam radius at the focal point was estimated to be 0.125 mm (Ref. 1). The ambient air temperature and pressure were taken to be 290 K and 1 atm, respectively.

Plasma Formation

Figure 3a illustrates the shape of the plasma formed at the end of the laser pulse. Figures 3b and 3c show the values of electron number density and the gas temperature along the axis of the laser beam at different times, where the laser light is propagating from left to right. The pressure profile in this case would look similar to the temperature profile, especially because there is not much variation in the total density in the first 20 ns. Notice that the plasma region is in the shape of a narrowband, stretched along the laser beam axis. Hence, we can characterize the plasma by length scale L_p, the length of the region which attains a certain minimum degree of ionization along the laser beam axis. L_p increases during the laser pulse emission as the plasma region expands from right to left (Figs. 3b and 3c). This is consistent with the energy absorption mechanism described in Ref. 7, where energy absorption starts in the narrowest region of converging laser beam and moves in the opposite direction of laser light propagation. This absorption wave leaves behind regions of high temperature and high degree of ionization. The plots also suggest that there is an upper limit to the values of temperature and electron density. This limit is imposed by the reflection parameters, as will be shown later.

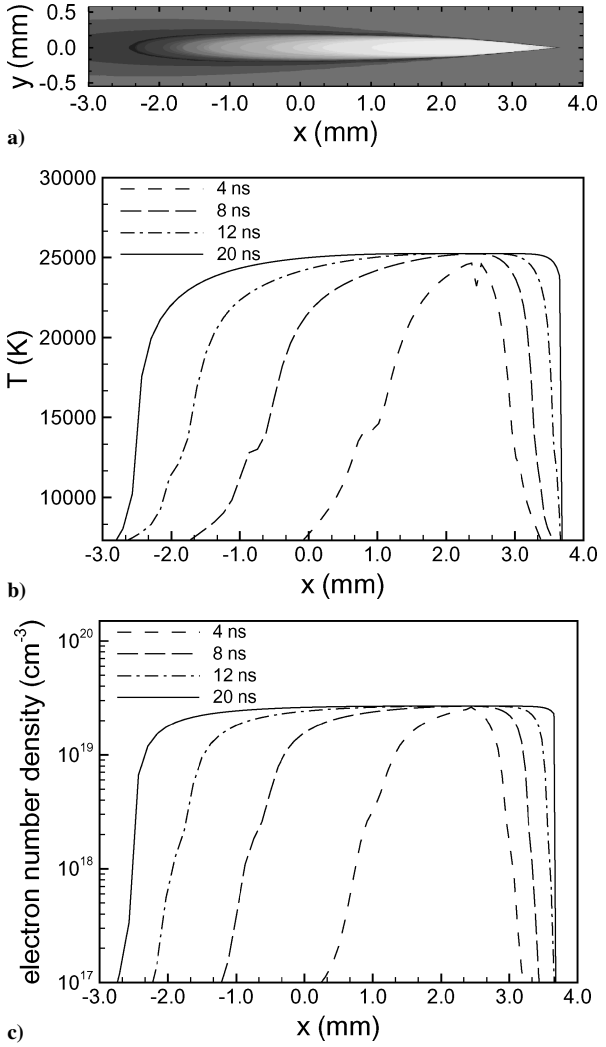

Fig. 3 Features of the laser spark: a) contours of gas temperature in the plasma region at 20 ns, b) gas temperature, and c) electron number density along the laser beam axis at various times.

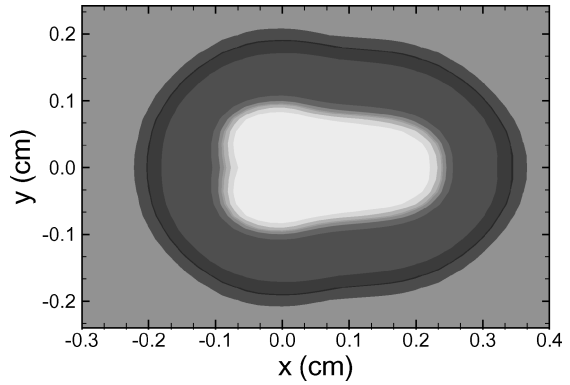

Fig. 4 Contours of temperature in the plasma region at 2 μs for laser energy deposition in quiescent air.

Figure 4 shows contours of temperature of the plasma region at 2 μs, and Fig. 5 plots the resulting pressure wave. The Rayleigh-scattering images of experiments[1] of laser-induced discharge in air from 2 to 30 μs are shown in Fig. 6. We observe that the shape of the simulated plasma region at 2 μs is similar to that of the experiments. Later at 5 μs, we see the pressure wave emerging from the plasma region. The pressure wave is initially elliptical in shape, but becomes spherical as it moves away from the central plasma region. We notice this feature in the experiments and as well as the

simulations. These qualitative comparisons show that the evolution of the plasma region in the computations is similar to that in the experiments. Note that, in Fig. 5, the two ellipse-shaped pressure contours at the center represent secondary pressure waves emerging from the plasma region at 5 μs. These pressure waves dissipate at later times.

Absorption and Reflection Parameters

The absorption parameter Q and reflection parameters A and B determine the shape and structure of the plasma region and the energy absorbed by it. Figure 7 shows the temperature in the plasma region along the axis of the laser beam for various values of absorptivity. As the absorptivity increases, the length of the plasma region also increases. This is expected because higher absorptivity enables regions with lower intensity of laser light in the focal volume to absorb more energy and ionize. Also, the region becomes more opaque and inhibits the growth of plasma near the focal point. Thus the value of Q determines the characteristic plasma length L_p.

Figure 8 shows the temperature in the plasma region along the axis of the laser beam for various values of reflectivity. The plots indicate higher temperatures for lower reflectivity. This is because reflectivity limits the extent of ionization in a region. Once the region has attained a certain degree of ionization, it becomes saturated and is incapable of absorbing any more radiation. Therefore, for given values of reflection parameters there is an upper limit to the temperature and degree of ionization that a region can achieve (see Figs. 3b and 3c). We can lower this limit by increasing the degree of reflectivity.

Grid Resolution and Electron Seeding

A uniform Cartesian grid was used for all computations. The grid spacing must be smaller than the laser beam radius at the focal point (0.125 mm), which is the smallest length scale in the geometry of the converging light. It is also necessary that the shape and structure of the plasma region are accurately simulated. It was discussed earlier that L_p is the characteristic length scale of the plasma region, and it has a unique value for given values of absorption and reflection

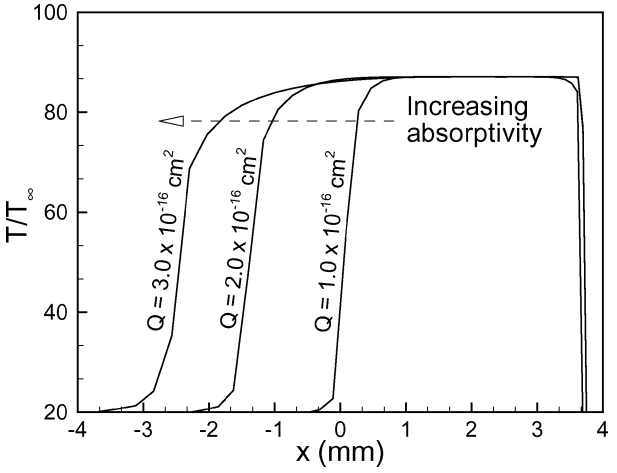

Fig. 7 Temperature in the plasma region along the laser beam axis for increasing absorptivity at 20 ns.

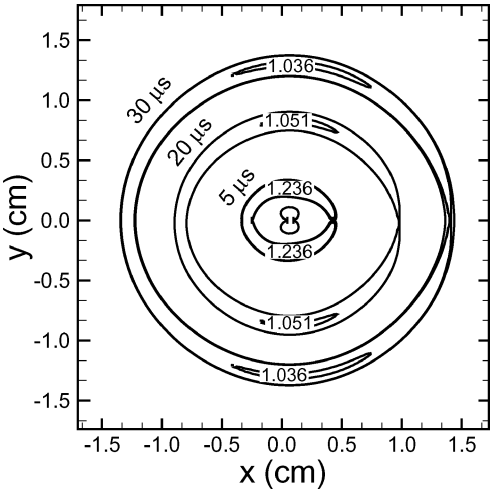

Fig. 5 Pressure wave (in atm) around the plasma region at various times after the laser energy deposition in quiescent air.

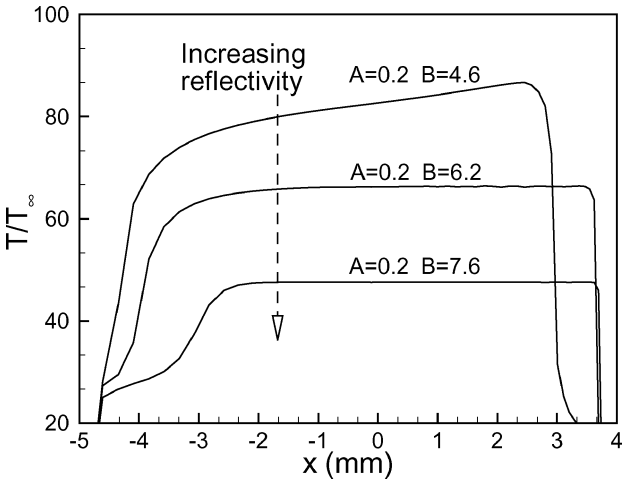

Fig. 8 Temperature in the plasma region along the laser beam axis for increasing reflectivity at 20 ns.

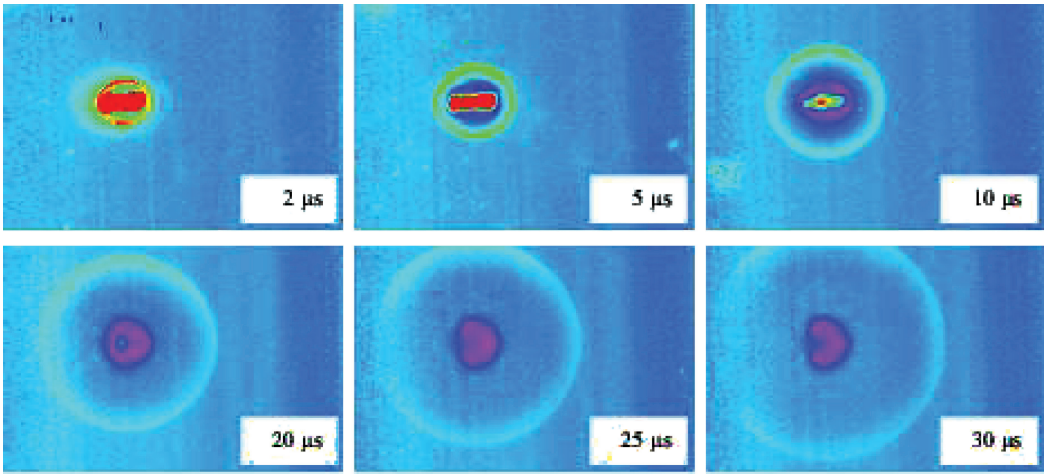

Fig. 6 Rayleigh scattering images for laser-induced discharge in quiescent air taken from Ref. 1.

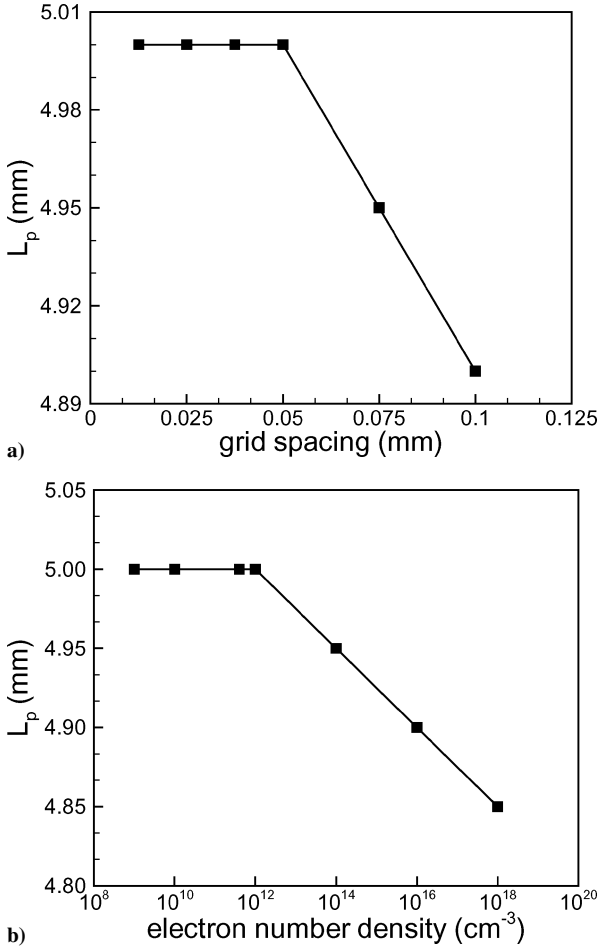

Fig. 9 Effect of a) grid resolution and b) electron seeding on the length of the plasma region.

parameters. Hence, we have performed a grid-convergence study to attain a constant value of L_p for fixed values of Q, A, and B. A 10% ionization fraction is used as a threshold to measure L_p here. Figure 9a shows that for grid sizes less than or equal to 0.05 mm L_p is a constant, implying that the grid provides sufficient resolution. Thus, we have chosen a grid size of 0.05 mm. Note that, as required, this grid size is also less than the laser beam radius at the focal point.

It was mentioned earlier that a small number of seed electrons are introduced to initiate the cascade ionization. To study the effect of this seeding on the solution, we have plotted L_p for different values of number density of the seed electrons, as shown in Fig. 9b. L_p remains constant for electron number densities below 10^{12} cm^{-3}, while it steadily decreases for higher electron number density. This is because high electron number densities enable regions with lower laser light intensity to absorb radiation and undergo cascade ionization before it occurs in the narrowest region of converging light. Transmission of laser light past this region is inhibited, shortening the length of the plasma region. Therefore we infer that the number density of the seed electrons does not affect the solution as long as cascade ionization begins in the narrowest region of the converging light.

Model Calibration

To calibrate the model, we need to determine the values of Q, A, and B. This was achieved by comparing the measurements of the flowfield (that follows the energy deposition) with the experiments.[1] The speed of propagation and the flow properties of the pressure wave, which emerges from the plasma region, depend on the amount of energy absorbed in the plasma region, which in turn is a function of Q, A, and B. Therefore, we can determine their values by matching the simulated flow features with the experiments.

Using the preceding methodology, the values were determined to be $Q = 3.0 \times 10^{-16}$ cm^2, $A = 0.3$, and $B = 4.6$. Figure 10 shows

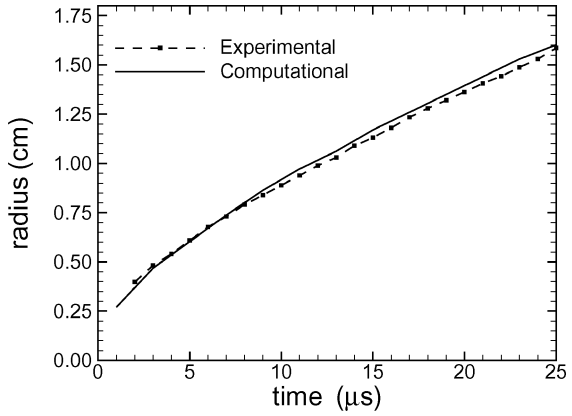

Fig. 10 Comparison of the variation of pressure wave radius with time between computational and experimental data[1] for laser energy deposition in quiescent air.

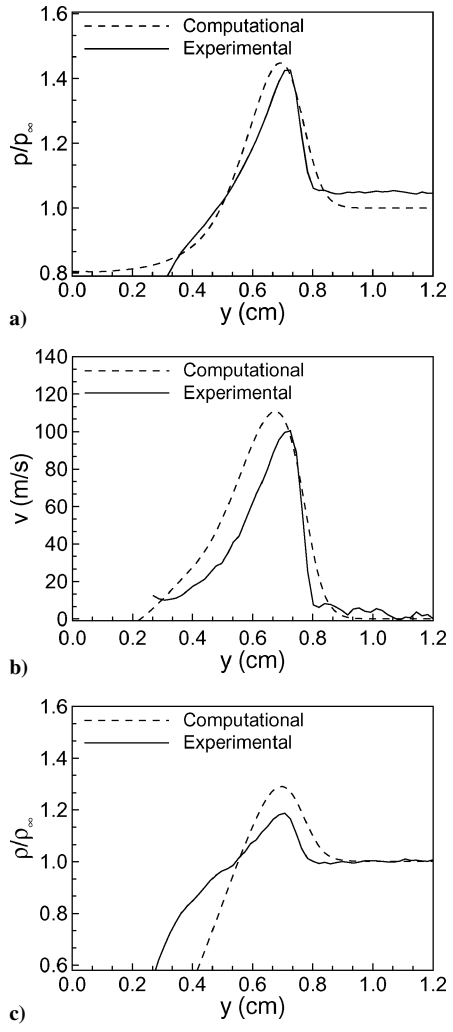

Fig. 11 Comparison of a) pressure, b) velocity, and c) density, along an axis perpendicular to the direction of laser propagation and passing through the center of the energy spot, between computational and experimental data[1] at 10 μs in quiescent air.

the comparison of the pressure wave radius with time, and Fig. 11 shows the comparison of pressure, velocity, and density of the flow along the radial direction at 10 μs. These plots indicate that, for the preceding values of Q, A, and B, the speed of propagation and flow properties of the pressure wave are in good agreement with experiments.

In the present case the pulse energy is 108 mJ; however, the model is designed such that the values of Q, A, and B are independent

of the pulse energy. The change in the pulse energy is accounted for by the variation in the input beam intensity. To support this claim, we have compared the energy absorbed by the plasma region in the simulations with experiments for a pulse energy of 180 mJ (Glumac, N., and Elliott, G., Univ. of Illinois, Urbana, IL, 2003). In the experiments, the energy of the laser beam was measured before and after it passed through the plasma region. The difference in these two measurements gave the approximate value of the energy absorbed by the plasma. (The actual value is less than this because of radiative losses.) The energy absorbed by the plasma region was 151 mJ for the experiments, and it was 153 mJ for the simulations, which is within 2% of the experimental value.

Here we have made use of the fluid-dynamic effects of energy deposition to calibrate the model. On the other hand, we have not made quantitative validation of features like distribution of temperature and the electron density in the plasma region during the nanosecond regime. But, because our work focuses on the fluid dynamic aspects of energy deposition in supersonic flows we believe that this method of calibration gives us sufficiently accurate values for flow control studies.

Energy Deposition in Supersonic Flows

Three-dimensional computational-fluid-dynamic simulations were performed to study the effect of energy deposition in blunt-body flows. Energy from a laser discharge was deposited upstream of a sphere in a steady supersonic flow. This was achieved by focusing a laser beam in front of the sphere, in a direction perpendicular to the flowfield. The flow conditions were chosen to simulate the experiments done at Rutgers University.[1] We have simulated energy deposition in two types of flows: supersonic flow past a sphere and flows with an Edney type IV shock–shock interaction on a sphere.

The timescale of the laser pulse is of the order of nanoseconds, while the timescale of the flow around the sphere is of the order of microseconds. Hence the process of laser energy deposition into the gas can be assumed to be independent of the supersonic flow. However, the evolution of this energy discharge region continues well into the microsecond range. Therefore, one has to account for the chemical reactions occurring in the plasma region while computing the flow. Taking these issues into consideration, the simulations were done in the following way. First, the steady-state supersonic flowfield was achieved using the same chemistry model that was used in the plasma formation case. Then the plasma formation and its evolution into a pressure wave in quiescent air were simulated until 0.5 μs. This was done on an axisymmetric domain. The resulting flowfield was then superimposed onto the three-dimensional steady supersonic flow by mapping the axisymmetric grid about the point of energy deposition onto the three-dimensional grid, as illustrated in Fig. 12. Note that the region of energy deposition is asymmetric about the horizontal plane.

Energy Deposition Upstream of Flow past a Sphere

The diameter of the sphere was set to 25.4 mm. The freestream Mach number was 3.45, stagnation pressure was 1.4 MPa, and stagnation temperature was 290 K. The laser pulse energy was 160 mJ, whereas the other laser beam parameters were the same as for the quiescent air case.

The interaction of the energy spot with steady supersonic flow is illustrated in Figs. 13 and 14, which show the pressure contours, surface pressure, and surface heat-transfer rate on the sphere. Initially, the energy spot is located upstream of the sphere in the steady flow. As the energy spot moves downstream, the resulting pressure wave expands into the surrounding flow and interacts with the bow shock in front of the sphere. This leads to an increase in surface pressure and heat-transfer rate, as seen at 25 μs in Fig. 14. The pressure wave is closely followed by the high-temperature spot, which causes the bow shock to bulge and move away from the sphere. At the same time, we observe a substantial decrease in surface pressure. The peak pressure decreases by 80% at 45 μs. Adelgren et al.[14] analyzed this interaction between the shock and the energy spot using a simplified one-dimensional analysis of a shock-wave interaction with a temperature discontinuity. Their analysis shows that the shock, which

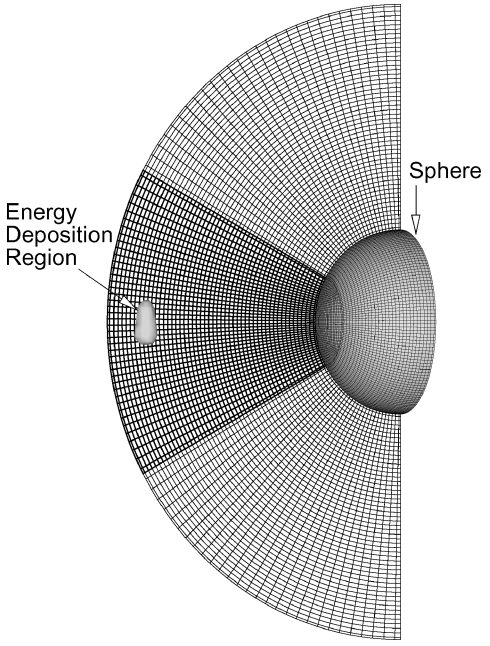

Fig. 12 Graphical representation of laser discharge region superimposed on the three-dimensional grid.

was stationary before the interaction, moves upstream, while an expansion fan moves downstream. This explains the low surface pressures and the bulging of the shock. The heat-transfer rate also decreases when the high-temperature spot reaches the bow shock. But once the spot moves past the bow shock and reaches the sphere, the temperature near the sphere increases, leading to a sharp increase in the heat transfer rate (four times the steady-state value). After this, the high-temperature region convects around the sphere, and the flow returns to its steady state. In summary, the effect of energy deposition on the sphere lasts for about 60 μs. During this time, the surface pressure is lower than the steady-state value, while the surface heat-transfer rate increases as well as decreases with respect to its steady-state value.

Figure 15 shows the peak temperature of the energy spot with time, until the spot comes in contact with the bow shock at 28 μs. Initially, the peak temperature of the energy spot is orders of magnitude higher than that of the surrounding flow. The high temperature leads to dissociation of air molecules and the presence of N, O and NO species in significant amounts. While the spot moves toward the sphere, its peak temperature decreases because of the work done in expanding the pressure wave against the ambient air pressure. The decrease in temperature leads to exothermic recombination of air, decreasing the chemical energy (T_c curve in Fig. 15) of the region. Thus, the recombination process results in transfer of stored chemical energy into translational energy while the spot is being convected by the flow. This energy release compensates for some of the expansion losses, sustaining the high-temperature region. In the absence of the stored chemical energy, the temperature of the energy spot would have decayed at a much faster rate. To demonstrate this, we have simulated the flow assuming a nonreacting perfect gas and plotted the corresponding temperature variation in Fig. 15. In this case, only the temperature and total pressure of the energy spot were superimposed, whereas the density was calculated by assuming a perfect gas. As expected, the temperature decreases at a faster rate than in the case of reacting flow because there is no chemical energy stored in this case. At 28 μs the peak temperature of the energy spot is 65% lower than that for the reacting flow case.

Energy Deposition in a Flow with Edney Type IV Shock–Shock Interaction

Edney type IV shock–shock interactions occur in a supersonic flow when an oblique shock impinges onto the bow shock in front of the leading edge of the sphere as shown in Fig. 16. This leads to

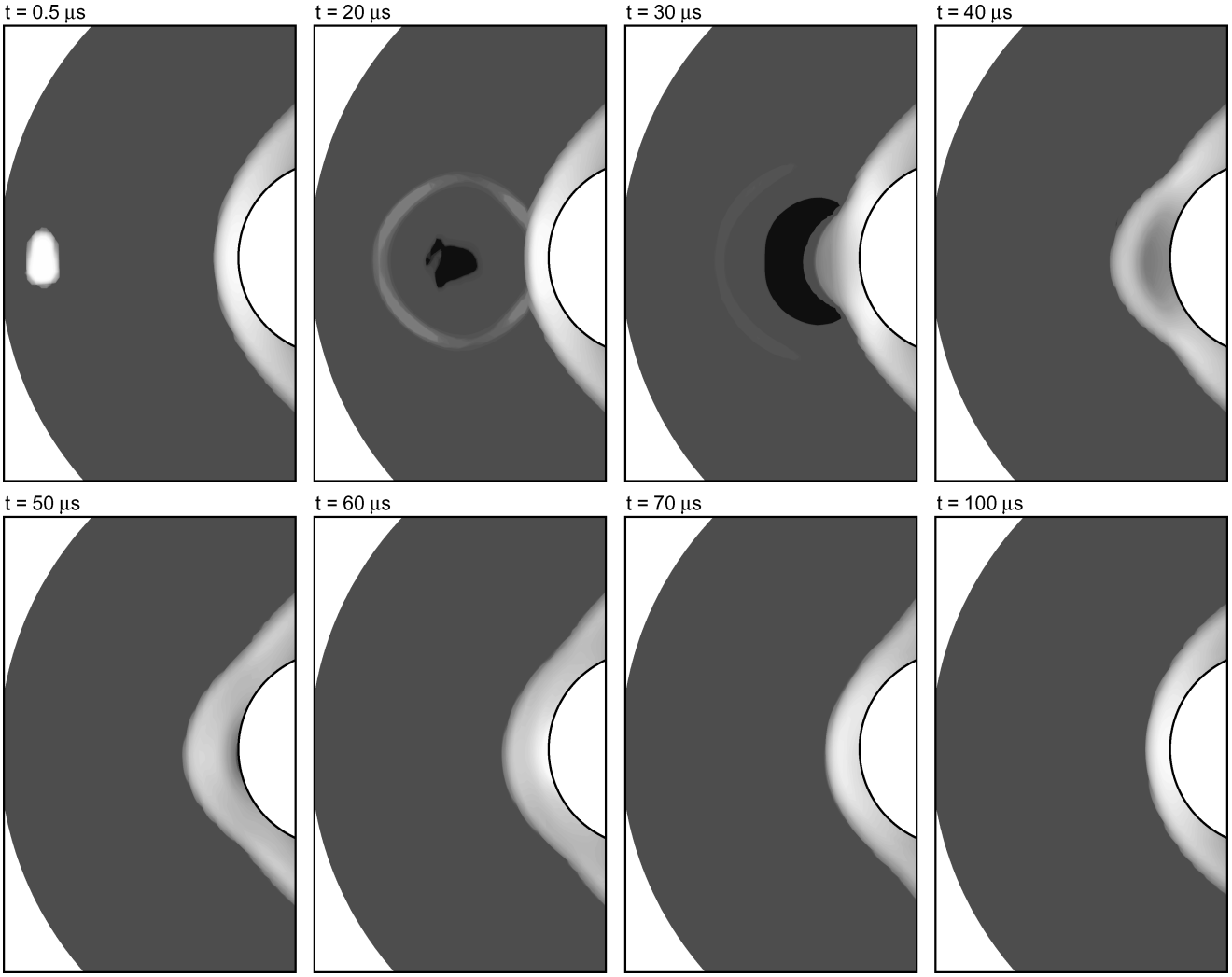

Fig. 13 Pressure contours for energy deposition in Mach 3.45 flow past a sphere at various times.

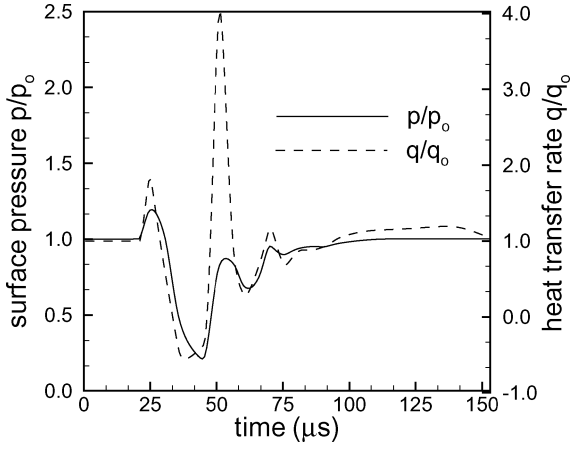

Fig. 14 Peak surface pressure and heat-transfer rate on the sphere, for energy deposition in Mach 3.45 flow past a sphere (p_0 and q_0 are the initial stagnation-point values).

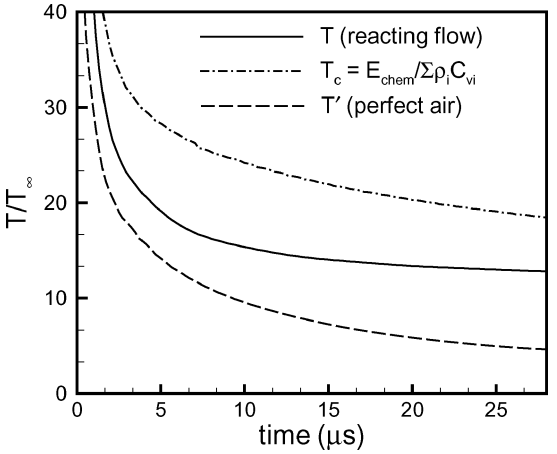

Fig. 15 Variation of temperature T and chemical energy T_c in reacting flow and variation of temperature T' in perfect air in the energy spot, before it reaches the bow shock, in Mach 3.45 flow past a sphere ($T_\infty = 89$ K).

high localized heat-transfer rate and surface pressure on the sphere, in the region just above the oblique shock. In our simulations, the oblique shock was assumed to propagate from an upstream wedge of 15 deg. The laser energy was deposited at different locations equidistant from the leading edge of the sphere as shown in Fig. 16. In the figure, β is the arc angle about the leading edge of the sphere, and it increases in the clockwise direction. The other flow conditions were the same as they were for the earlier case.

Figure 17 shows the pressure contours of the energy spot interaction with the flow, and Fig. 18 shows the variation of peak surface pressure and heat-transfer rate during the interaction. As the energy spot moves downstream, the high-temperature region changes the local Mach number and deforms the oblique shock ($t = 20$ μs in Fig. 17). Once the energy spot approaches the shock structure, the subsequent flow behavior is similar to that observed in the case of flow past a sphere. The pressure wave around the energy spot comes

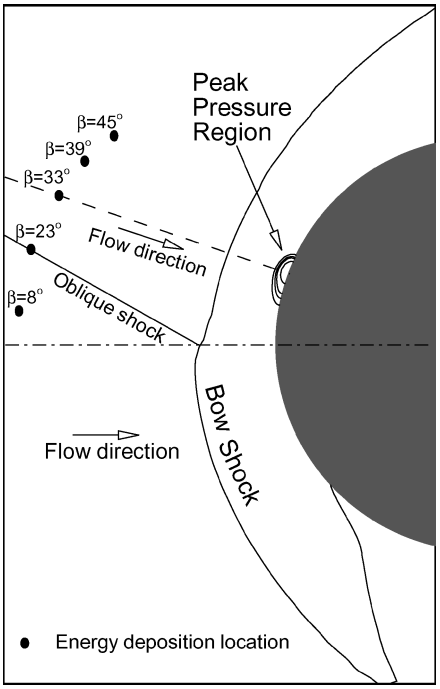

Fig. 16 Schematic showing Edney type IV shock–shock interaction (Mach 3.45 flow with 15-deg flow turn angle) along with the initial location of the energy deposition regions.

in contact with the shock structure and increases the peak surface pressure and heat-transfer rate. The pressure wave is followed by the high-temperature region, which causes the shock to bulge decreasing the surface pressure and heat-transfer rate. Next, the energy spot moves past the shock and reaches the sphere, increasing the temperature in that region. This leads to an increase in the surface heat-transfer rate. Finally, the shock structure returns to the steady state.

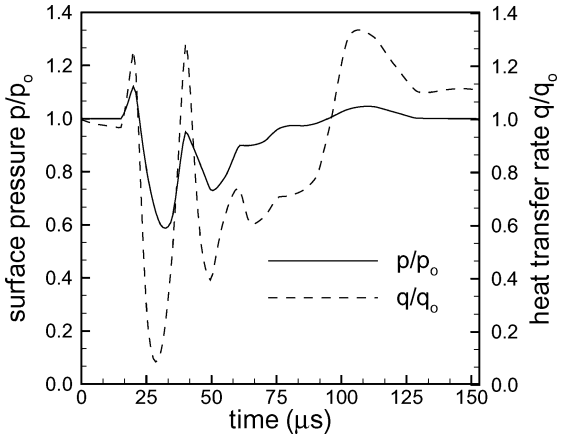

Fig. 18 Peak surface pressure and heat-transfer rate on the sphere, for energy deposition in a flow with Edney type IV shock–shock interaction. (Mach 3.45 flow with 15-deg flow turn angle; p_0 and q_0 are the initial stagnation-point values.)

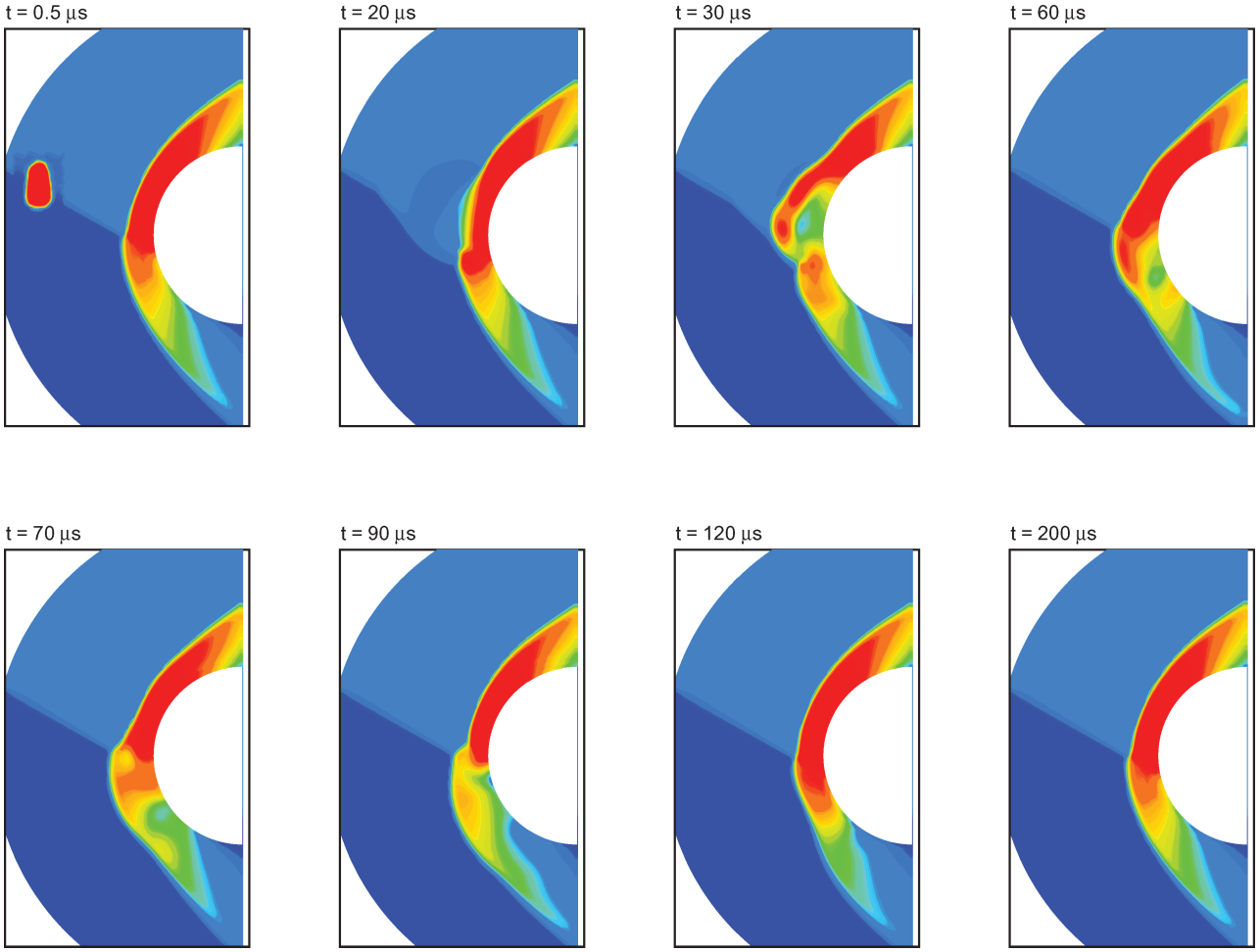

Fig. 17 Pressure contours for energy deposition in a flow with Edney type IV shock–shock interaction (Mach 3.45 flow with 15-deg flow turn angle) at various times.

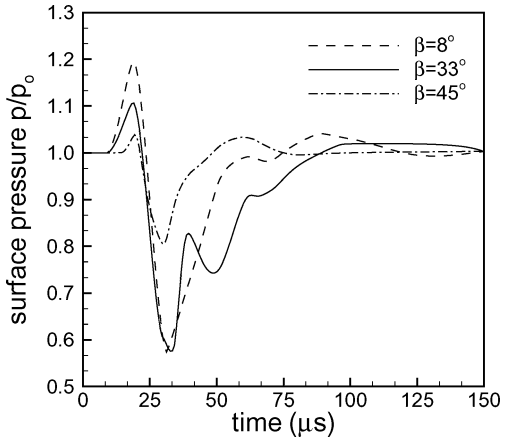

Fig. 19 Effect of the location of energy deposition on the peak surface pressure in a flow with Edney type IV shock–shock interaction. (Mach 3.45 flow with 15-deg flow turn angle; p_0 is the initial stagnation-point value.)

The simulations were performed for the various energy deposition locations given in Fig. 16. Figure 19 plots the variation of the peak surface pressure with time for three of these locations. The figure shows significant differences between the values for different cases, suggesting that the location of energy deposition can be optimized to obtain maximum pressure reduction. Hence, we have computed the time-averaged peak surface pressure (during the interaction of the energy spot with the flow) for all of the energy deposition locations and found that the maximum reduction in average peak pressure occurs for $\beta = 33$ deg. The reason for this can be deduced from the fact that the line joining this location and the core of the peak pressure region on the sphere (dashed line in Fig. 16) is parallel to the flow direction. In this case, the flow convects the energy spot directly onto the peak pressure region, making it most effective.

Conclusions

We have performed a computational study of laser energy deposition in supersonic flows as a means of localized flow control. For this purpose, a laser energy deposition model was developed. This model captures the energy absorption mechanism by using the concepts of absorption and reflection of laser light. An 11-species finite-rate chemical kinetics model was used to simulate the air breakdown. The shape of the plasma region and the resulting pressure wave were found to be in good agreement with the experiments. The values of absorption and reflection parameters were found to affect the shape and structure of the plasma region and the energy absorbed. These values were determined by using experimental flowfield measurements. The independence of the absorption and reflection parameters from the input laser pusle energy was verified. This was done by showing that the energy absorbed by the calibrated model agreed well with the experiments when the pulse energy was varied. The model was used to simulate energy deposition in steady supersonic flows past a sphere. The simulations show that during the convection of the energy spot downstream the chemical energy in the region sustains the high temperatures. The energy spot affects the shock structure, leading to a decrease in the peak surface pressure and the peak surface heat-transfer rate. The surface-pressure reduction is sustained until the flow returns to the steady state, but the reduction in surface heat-transfer rate does not last as long. In the case of flows with Edney type IV shock–shock interaction, maximum reduction in the peak surface pressure occurs when the energy spot is located at $\beta = 33$ deg. This is because, at this angle, the spot is convected onto the region with the maximum surface pressure on the sphere. In future studies, we will examine the effects of multiple laser pulses and higher flow Mach numbers on flow control.

Acknowledgments

This research is supported by Air Force Office of Scientific Research (AFOSR) under Grant F49620-01-1-0368. The views and conclusions contained herein are those of the authors and should not be interpreted as necessarily representing the official policies or endorsements, either expressed or implied, of the AFOSR or the U.S. Government.

References

[1]Adelgren, R. G., Elliott, G. S., Knight, D. D., Zheltovodov, A. A., and Beutner, T. J., "Energy Deposition in Supersonic Flows," AIAA Paper 2001-0885, Jan. 2001.

[2]Riggins, D. W., Nelson, H. F., and Johnson, E., "Blunt-Body Wave Drag Reduction Using Focused Energy Deposition," *AIAA Journal*, Vol. 37, No. 4, 1999, pp. 460–467.

[3]Phuoc, T. X., "Laser Spark Ignition: Experimental Determination of Laser-Induced Breakdown Thresholds of Combustion Gases," *Optics Communications*, Vol. 175, No. 4, 2000, pp. 419–423.

[4]Molina-Morales, P., Toyoda, K., Komurasaki, K., and Arakawa, Y., "CFD Simulation of a 2-kW-Class Laser Thruster," AIAA Paper 2001-0650, Jan. 2001.

[5]Wang, T. S., Chen, Y. S., Liu, J., Myrabo, L. N., and Mead, F. B., "Advanced Performance Modeling of Experimental Laser Lightcrafts," AIAA Paper 2001-0648, Jan. 2001.

[6]Radziemski, L. J., and Cremers, D. A., *Laser-Induced Plasmas and Applications*, Marcel Dekker, New York, 1989, Chaps. 1 and 2.

[7]Raizer, Y. P., "Breakdown and Heating of Gases Under the Influence of a Laser Beam," *Soviet Physics USPEKHI*, Vol. 8, No. 5, 1966, pp. 650–673.

[8]Dewhurst, R. J., "Comparative Data on Molecular Gas Breakdown Thresholds in High Laser-Radiation Fields," *Journal of Physics D: Applied Physics*, Vol. 11, No. 16, 1978, pp. L191–L195.

[9]Laux, C., Pierrot, L., Gessman, R., and Kruger, C. H., "Ionization Mechanisms of Two-Temperature Plasmas," AIAA Paper 99-3476, June 1999.

[10]Nagulapally, M. K., "Modeling of Discharges in Flowing Plasmas," Ph.D. Dissertation, Dept. of Aerospace Engineering and Mechanics, Univ. of Minnesota, Minneapolis, MN, June 2000.

[11]Candler, G. V., and MacCormack, R. W., "Computation of Weakly Ionized Hypersonic Flows in Thermochemical Nonequilibrium," *Journal of Thermophysics and Heat Transfer*, Vol. 5, No. 3, 1991, pp. 266–273.

[12]Mitchner, M., and Kruger, C. H., *Partially Ionized Gases*, Wiley, New York, 1973, pp. 92–94.

[13]Lee, J. H., "Electron-Impact Vibrational Relaxation in High-Temperature Nitrogen," AIAA Paper 92-0807, Jan. 1992.

[14]Adelgren, R. G., Yan, H., Elliot, G., Knight, D. D., Beutner, T. J., Zheltovodov, A. A., Ivanov, M., and Khotyanovsky, D., "Localized Flow Control by Laser Energy Deposition Applied to Edney IV Shock Impingement and Intersecting Shocks," AIAA Paper 2003-0031, Jan. 2003.

M. Auweter-Kurtz
Associate Editor